Shrink-Film Configurable Multiscale Wrinkles for Functional Alignment of Human Embryonic Stem Cells and their Cardiac Derivatives

Aaron Chen, Deborah K. Lieu, Lauren Freschauf, Valerie Lew, Himanshu Sharma, Jiaxian Wang, Diep Nguyen, Ioannis Karakikes, Roger J. Hajjar, Ajay Gopinathan, Elliot Botvinick, Charless C. Fowlkes, Ronald A. Li, and Michelle Khine**

Studies of cellular responses to topographies ranging from nano- to microscales are of great importance to fundamental cell biology as well as to applications in stem cell biology and tissue engineering.[1–3] Leveraging traditional fabrication techniques originally developed for the semiconductor industry, researchers have been able to precisely control the topographical features of in vitro substrata to better understand the interaction between cells and their microenvironments. Previous studies have demonstrated the phenomenon of contact guidance, directed alignment and migration along lines of topographic anisotropy, using a variety of cells—from myocytes to adult stem cells—with a range of responses.[3–6] For example, the effects of contact guidance have been shown to induce cytoskeletal rearrangement, nuclear deformation, and gene expression changes in fibroblasts.[4] In addition, stem cell fate can be solely determined by the mechanical cues of their microenvironment in the absence of soluble factors.[6–10] Therefore, the substrates used for such studies need to be biologically relevant and mimic the in vivo microenvironment.

While it has been shown that biophysical cues of various length scales affect cells differently,[2–4] the majority of currently available fabricated topographies have simple and repetitive patterns of grooves or ridges of either a homogenous size or of a narrow size range at either the microscale, or more recently, the nanoscale.[1,5,11–15] Although such designs are helpful in studying a controlled cellular behavior, they do not represent the physiological conditions of native tissue necessary for tissue engineering. Nature's ordering is dramatically different from the precisely periodic arrays produced from high precision fabrication approaches. In vivo, the organization of the extracellular matrix (ECM) varies dramatically in its structural arrangement, content, texture, and fiber bundle thickness. For example, collagen, the main structural component in ECM, form self-similar fibrils (20–100s of nm), which in turn form bundles and fibers across several orders of magnitude.[16] While cells in vivo experience topographies with features across a vast size range, physiologically comparable cellular environments with length scales that span several orders of magnitude have not been readily simulated by precision micro- or nanofabrication techniques. Achieving such multiscale features typically relies on substantial capital equipment and/or fabrication expertise[2,17] limiting their accessibility to biological laboratories.

To address these challenges, we introduce an ultrarapid, tunable, robust, facile, and inexpensive fabrication method to create multiscaled self-similar alignment grooves ranging from nano- to micrometers as biomimetic cell culture substrates.

A. Chen, H. Sharma, Prof. M. Khine
Department of Chemical Engineering and Material Science
University of California
Irvine, Irvine, CA 92697, USA
E-mail: mkhine@uci.edu

Dr. D. K. Lieu
Department of Internal Medicine
Division of Cardiovascular Medicine
University of California
Davis, Davis, CA 95616, USA

L. Freschauf, V. Lew, D. Nguyen, Prof. E. Botvinick,
Prof. C. C. Fowlkes, Prof. M. Khine
Department of Biomedical Engineering
University of California
Irvine, Irvine, CA 92697, USA

J. Wang, Prof. R. A. Li
Stem Cell & Regenerative Medicine Consortium
LKS Faculty of Medicine
The University of Hong Kong
Pokfulam, Hong Kong
E-mail: ronald.li@mssm.edu

J. Wang, Dr. I. Karakikes, Prof. R. J. Hajjar, Prof. R. A. Li
Cardiovascular Research Center
Mount Sinai School of Medicine
New York, NY 10029, USA

Prof. A. Gopinathan
School of Natural Sciences
University of California
Merced, Merced, CA 95344, USA

Prof. C. C. Fowlkes
Department of Computer Science
University of California
Irvine, Irvine, CA 92697, USA

Prof. R. A. Li, Heart, Brain
Hormone & Healthy Aging Research Center
Department of Medicine and Physiology
LKS Faculty of Medicine
University of Hong Kong, Hong Kong

DOI: 10.1002/adma.201103463

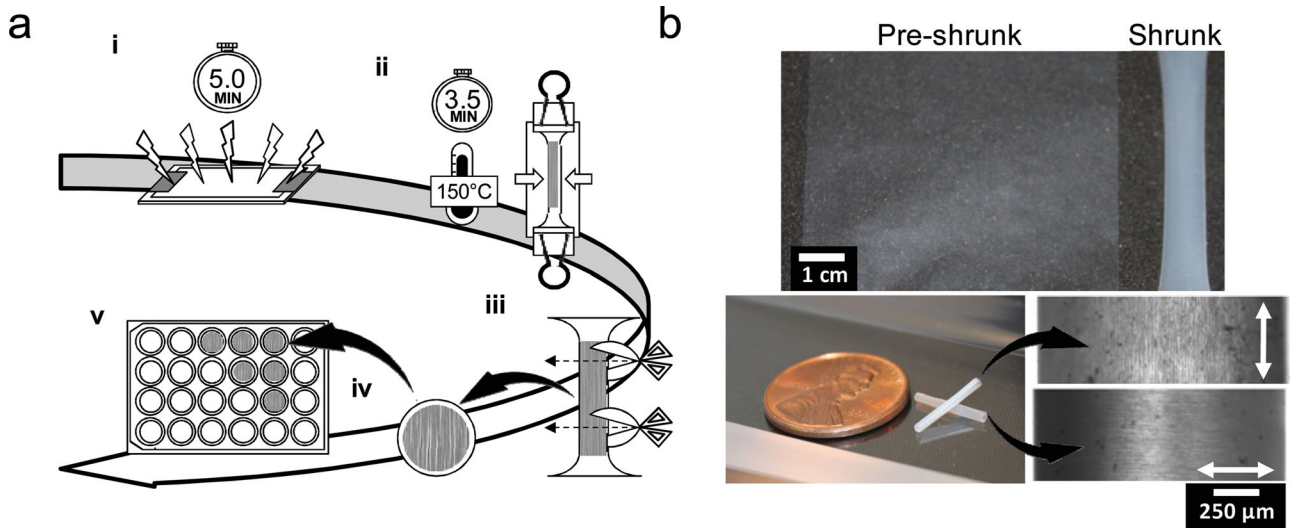

Figure 1. a) Process flow of shrink-film wrinkle formation. i) PE film is treated with oxygen plasma for 5 min (P5). ii) PE film is constrained on opposite sides and thermally shrunk to create unidirectional wrinkles. iii) Shrunk PE film is cut into desired dimension and iv) mounted onto a glass coverslip (v) to be used in cell culture experiment. b) Preshrunk (left) and shrunk (right) films. Upon heating, the PE film will shrink approximately 90% lengthwise. Inset shows the P5 condition rolled-up into tubes. The direction of wrinkles can be either parallel or perpendicular to the long axis of the tube. Bright field microscopy images taken from the tubes illustrate the direction of wrinkles. Images are taken at 4× magnification.

Commodity shrink film, prestressed polyethylene (PE) (0.5 mil gauge), is oxidized and subsequently shrunk uniaxially to create aligned grooves, or "wrinkles" (**Figure 1**a), over relatively large areas of clinically relevant size (1 cm × 6 cm), which is difficult to achieve with other approaches such as electron-beam (e-beam) lithography or nanoimprint lithography (Figure 1b). In contrast, our patterned size is only limited by the size of the plasma chamber and is amenable to large-scale roll-to-roll plasma systems. Instead of depositing nanometric layers of metal by e-beam or sputter coating in order to generate the stiffness mismatch to create wrinkles upon the retraction of the shrink film as previous reported,[18,19] we have now obviated the need for a metal layer altogether. Unlike silicon, polydimethylsiloxane (PDMS), or glass substrates, this thermoplastic substrate can also be easily heat-molded into various nonplanar shapes such as tubes to serve as 3D scaffolds for studying endothelial alignment for blood vessels (Figure 1b).

Oxidation is achieved by oxygen plasma treatment, which creates a thin and relatively stiff layer at the surface of bulk PE film. Leveraging the inherent retraction properties of the prestressed film, which shrinks uniaxially by 90% by heating briefly to 150°C, this mismatch in stiffness causes the stiff outer oxidized layer to buckle and form predictably controllable distributions of nano- and microwrinkles (**Figure 2**a).[18] Complete fabrication of the topographical substrate takes less than 10 min. The properties of the aligned wrinkles can be controlled through the plasma treatment time. Interestingly, self-similar wrinkles form across various length scales with bundling of the wrinkles apparent at longer oxidation times. The multiscale hierarchy is revealed through various scanning electron microscopy (SEM) image magnifications. At lower magnification, in which the smaller wrinkles cannot be resolved, the apparent predominant wavelength (major wrinkles) range shifts from 1 to 7 µm as plasma treatment time increases from 1 to 15 min (Figure 2a). At higher magnification, the apparent predominant wavelengths (minor wrinkles) are 380, 100, and 200 nm with shoulder peaks at 200, 60, and 150 nm for the 1 (P1), 5 (P5), and 15 (P15) min plasma treatment conditions, respectively (P1 and P15 data not shown). The formation of aligned hierarchical grooves is due to different generations of effective layers that are thicker and stiffer than the previous layer.[20] Upon shrinking, the first generation of wrinkles and a new effective layer form. Further shrinking induces formation of a new generation of wrinkles until the shrinking process is complete. This process forms multiscale grooves as each successive generation of wrinkles form with wavelengths similar to the hierarchical structuring of collagen bands.[16] The data from Figure 2a reveal that there are at least two generations of P5 wrinkles. As is apparent from the graph, and confirmed by the atomic force microscopy (AFM) measurements (Supporting Information Figure 1), a nested hierarchy is apparent at the 5 and 15 min plasma times, with distinct size populations. In addition, AFM measurements confirm that the thin layer of Matrigel coating was conformal to the wrinkles and did not obscure substrate topography (Figure 2b). The distribution of wrinkles is controllable, with larger wrinkle sizes becoming more dominant with increased plasma time, in agreement with our theoretical model based on skin thickness.[18] At 1 min, we suspect the larger wrinkles and lack of bundling is due to an insufficiently thick and stiff outer layer. The average depths of wrinkles are 159 nm, 247 nm, 310 nm, and 233 nm for P1, P5, P5 with Matrigel coating, and P15, respectively (Figure 2b). Since the wrinkles are multiscale, the range of depth spans several order of magnitudes.

To evaluate the effectiveness of contact guidance using these biomimetic wrinkles, we align mouse embryonic fibroblasts (MEFs), aortic smooth muscle cells (AoSMCs), and human embryonic stem cells (hESCs). The wrinkles can be directly coated with ECM for cell culture or, alternatively, used as a mold for various tissue engineering biodegradable polymers. Growth arrested MEFs are grown on glass coverslip, P0 (no

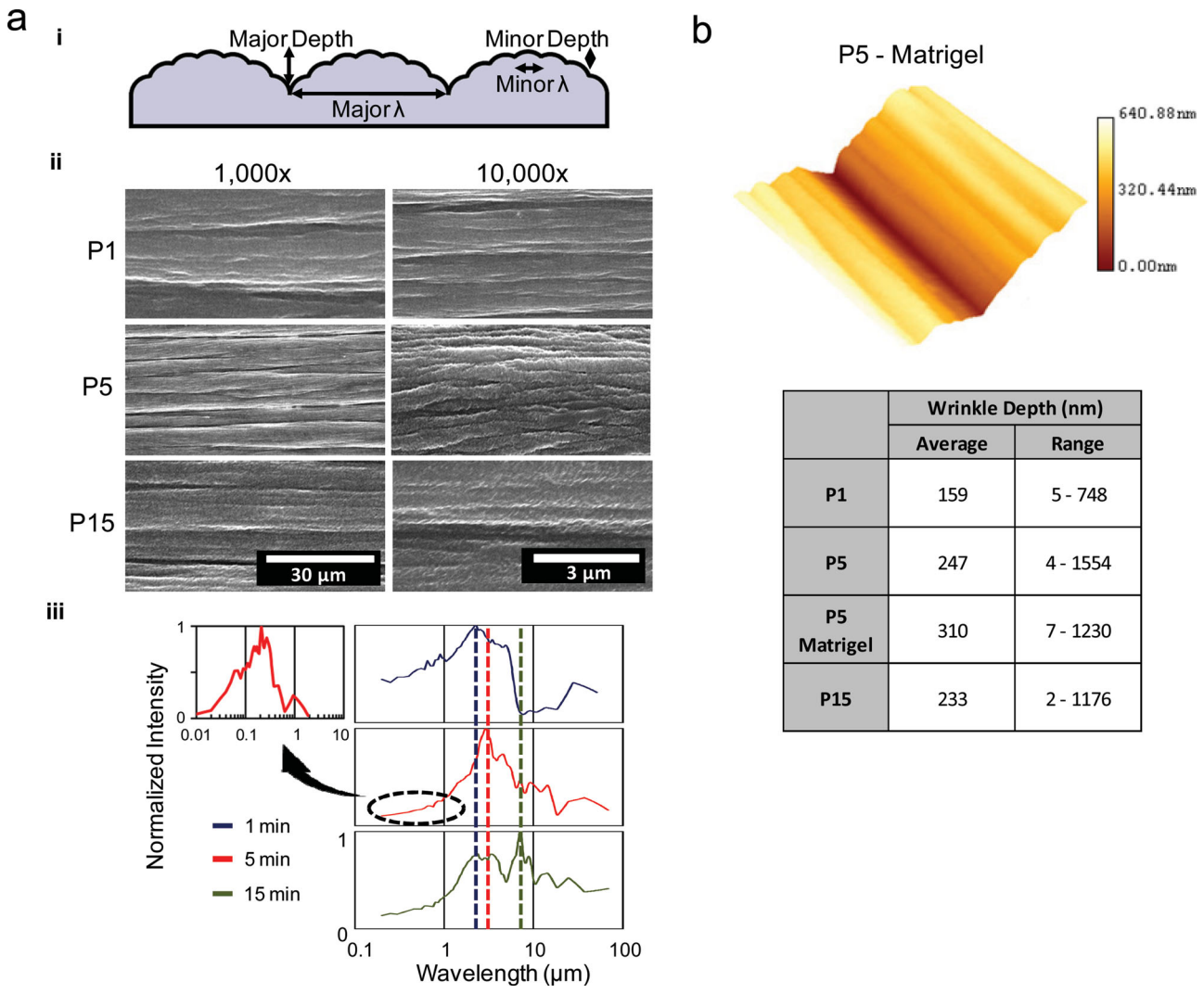

	Wrinkle Depth (nm)	
	Average	Range
P1	159	5 - 748
P5	247	4 - 1554
P5 Matrigel	310	7 - 1230
P15	233	2 - 1176

Figure 2. a) i) Schematic of wrinkle formation. Two generations of heirarchical wrinkles are demonstrated in the diagram. The black outline represents the stiff outer layer and the color represents the soft bulk polymer. ii) SEM images with progressive zooms of 1000× and 10 000×, illustrating the self-similar wrinkles for P1, P5, and P15 conditions. The bundling of the wrinkles is apparent. iii) Feature scale distribution estimated from the Fourier transform of SEM images for the three different plasma conditions. Inset shows the smaller population of wrinkles at 20 000×, not resolvable at the lower SEM magnification. b) AFM indicates the bundles and the height range of the wrinkles. The AFM image demonstrates the Matrigel coating conform to the topography of the P5 wrinkled substrate. The scan distance of the AFM image is 5 × 5 µm^2. The table summarizes the average and the range wrinkle depths for P0, P1, P5 with and without Matrigel coating, and P15.

plasma treatment), P1, P5, and P15 substrates for 24 h. Six substrates per condition are included to ensure the consistency of data. F-actin is stained to visualize cytoskeleton of MEFs. MEFs grown on both glass coverslip and P0 exhibit random contact guidance, whereas MEFs grown on the P1, P5, and P15 substrates align within 24 h (**Figure 3**a). Moreover, more cells are aligned on the P5 than those grown on the P1 and P15, as indicated by the orientation distribution polar plots. This is likely due to the range of P5 wrinkles (60 nm to 3 µm), which is similar to that of natural ECM fibrils. Therefore, the P5 substrate is chosen for the subsequent AoSMC and hESC alignment experiments.

While there has been a report that hESCs align to 600 nm grooves in the presence of differentiation media,[21] the ability to align and maintain the pluripotent hESCs on the wrinkles without differentiation media over time is important for established differentiation protocols that require an expansion phase of pluripotent hESCs.[22,23] Despite the mechanical cues sensed by the hESCs, the cells remain relatively pluripotent over time when cultured on the wrinkled substrate under feeder-free pluripotent conditions (Supporting Information Figure 2).[24] On both days 3 and 6, healthy hESCs suspended as single cells (Supporting Information Figure 2b, P1 gate) grown on both control and wrinkles express TRA-1-81, a pluripotent surface marker. Notably, forward and side scattering data from flow cytometry indicate that the cells grown on the wrinkled substrate remain healthier than those grown on the controls (Supporting Information Figure 2b). The

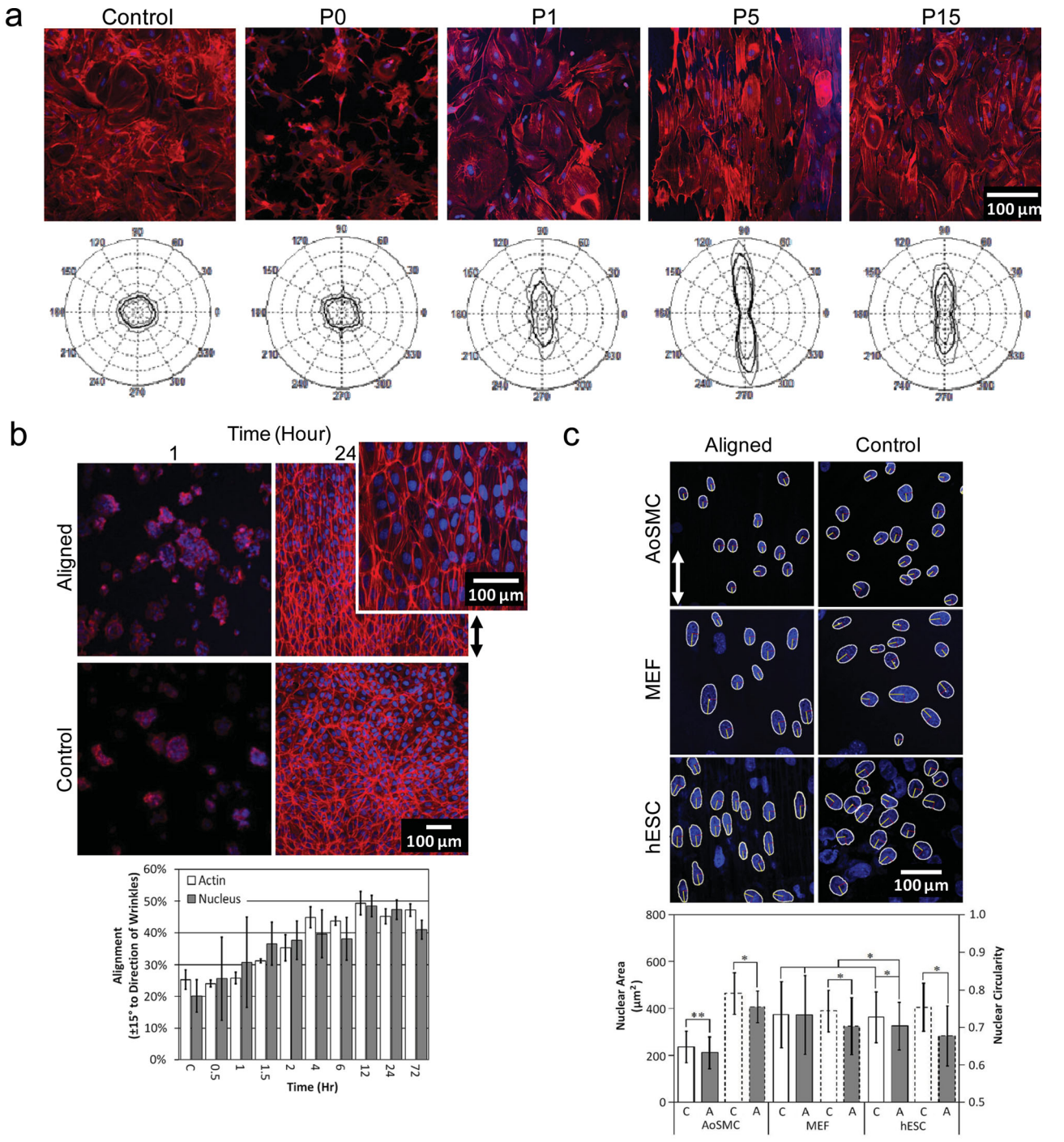

Figure 3. Alignment of various types of cells on the wrinkles. a) Fluorescent microscopy images of MEFs cultured on control (glass slide), P0, P1, P5, and P15 wrinkled substrates for 24 h. The polar plots reveal orientation distribution of f-actin for cells grown on different substrates. Each plot is an average of 6 replicates and 30 images total. 90° and 270° are the direction of wrinkles. Thinner lines indicate standard deviation. b) Subcellular hESC alignment as indicated by time lapse f-actin and nuclei alignment over 72 h (bar graph, mean ± standard deviation (s.d.), $n = 9$ images per time point). Control, C, represents cells grown on glass coverslip, and it is an average of all controls from all time points ($n = 81$ images). c) Nuclear deformation as indicated by nuclear area (left axis of graph, solid line) and circularity (right axis of graph, dash line) as compared to other cell types including AoSMCs and MEFs. Bar graph represents mean ± s.d., $n = 9$ images (>300 nuclei) per time point, and $*p < 0.001$ and $**p < 0.01$. For (b) and (c), red is f-actin (rhodamine) and blue denotes nuclei (DAPI).

increase in side scattering of the same cell type over time typically indicates a less healthy state of cells, which corresponds to an increase in cellular surface granularity and internal complexity. With increasing culture time, more cells shift into the high side scattering region for both controls and wrinkles; however, the percent of cells remaining in P1 is considerably

higher for cells grown on wrinkles (17.4%) than those grown on the controls (6.4%).

We demonstrate for the first time the subcellular time-lapse response to topography of feeder-free pluripotent hESCs without soluble differentiation factors. The alignment is assessed based on f-actin and nuclear alignment (Figure 3b). Time lapse imaging of the cells indicate that the majority of cells align to the wrinkles within the first 4 h of plating, with more than 40% of the cells stably aligning to within 15° of the wrinkle direction. As a point of comparison, to achieve roughly the same degree of alignment by flow with endothelial cells requires 1.5 Pa shear stress for 10 h.[25] The hESC nuclei are also more aligned compared to a study of fibroblast nuclei on 12.5 μm × 2 μm microgrooved topography at 24 h culture time.[4]

Notably, we demonstrate for the first time the deformation of pluripotent hESC nuclei due to topography. The deformed nuclei of hESCs exhibit a decreased surface area, in agreement with topography-induced direct mechanotransduction.[26] The nuclei of undifferentiated stem cells are more mechanically plastic than those of differentiated cells and change as a function of differentiation.[5,27] We reveal the highly compliant nuclei of hESCs through the measurements of nuclear area and circularity as compared to AoSMCs and MEFs (Figure 3c). The hESCs exhibit both a decreased average projected area, from 365 to 325 μm^2, as well as a decreased average circularity index, from 0.75 to 0.65, in response to the alignment ($p < 0.001$); this is in stark contrast to MEF, where nuclei circularity are altered ($p < 0.001$) by the wrinkles but their projected area are not affected. As apparent from the graphs, AoSMC nuclei do deform ($p < 0.01$ for projected area and $p < 0.001$ for circularity), but to a lesser degree compared to the more plastic undifferentiated hESC nuclei.

Understanding how the cell perceives topographical cues and translates that information to the nucleus to commence mechanotransductive signaling could enable a strategy of controlled stem cell differentiation without the need for either invasive stimuli or chemical inducement with defined media.[28] Importantly, because the multiscale topography inherent to this substrate is easily tuned by plasma treatment time, it is possible to map the effect of local topography on subcellular responses (Supporting Information Figure 3). This would allow, for example, the role of each length scale in contact guidance to be elucidated. Because comparatively little is yet understood with respect to the effects of hESC alignment on differentiation, it is important and now practical to test the range of physiologically relevant cues in a comprehensive format reflective of the multiscales typical of in vivo substrata.

After successfully aligning a variety of cells, we next test whether physiological functionality improves with alignment. To the best of our knowledge, the characterization of the electrophysiology of aligned hESC-derived cardiomyocyte (hESC-CM) monolayer by measuring action potential (AP) propagation using an optical mapping technique is demonstrated the first time. In the native heart tissue, alignment of cardiomyocytes contributes to the anisotropic tissue structure and facilitates coordinated mechanical contraction and electrical propagation. The alignment of cardiac muscle cells has been studied previously using various microfabrication techniques;[3,29,30] however, typical patterned substrates used in the tissue engineering do not exhibit the relevant physiological multiscale topographies. Previously, we demonstrated the alignment of murine neonatal cardiomyocytes (NNCMs) and hESC-CMs on PDMS substrates molded from metallic wrinkles by fluorescent staining of the nuclei, actin, and cardiac troponin.[19] Furthermore, the staining of connexin-43, a gap junction protein, revealed that the aligned NNCMs exhibited a more defined and consistent network than the unpatterned cells suggesting a more natural arrangement of native CMs. This hypothesis is corroborated by the measurement of alignment and AP propagation of hESC-CM monolayer. The alignment of hESC-CM monolayer is determined through f-actin stain, and the sarcomeric striation is revealed with orientation perpendicular to the wrinkles (**Figure 4**a). The arrangement of sarcomeric structures is more apparent and organized for the aligned cells than the unpatterned ones. For cells grown on the P0 and P5 substrates, 22 ± 2% and 45 ± 8% of the cells align to ±15° of the wrinkles on day 2, respectively. Furthermore, the alignment of the hESC-CM monolayer remains relatively unchanged until day 7. The aligned hESC-CM monolayer also exhibits a more synchronized contraction than the unpatterned one on day 2 (Supporting Information Movie 1 and 2). AP propagates across the monolayer grown on the control (P0) substrate expands uniformly away from the point of stimulation with an average conduction velocity of 2.13 ± 0.11 cm s^{-1}, which is similar to the value we previous reported (Figure 4 and Supporting Information Movie 3).[31] In contrast, the aligned monolayer exhibits an anisotropic propagation with faster longitudinal conduction velocity (LCV, 1.82 ± 0.20 cm s^{-1}) parallel to the direction of wrinkles than that of the transverse conduction velocity (TCV, 0.95 ± 0.08 cm s^{-1}) (Supporting Information Movie 4), giving rise to an anisotropic ratio (LCV/TCV) of 1.92 ± 0.20 (vs. 1.00 ± 0.05 of P0). The slower LCV is likely related to the morphology of the hESC-CM monolayer, which is a consequence of the size and depth of the wrinkles. Previously, Kim et al. demonstrated that the LCV of aligned neonatal rat ventricular myocytes is slower than that of unpatterned cells when the ridge, groove, and depth of the anisotropically nanofabricated substratum (ANFS) are 150, 50, and 200 nm, respectively,[3] and tuning of the dimensions of the ANFS can affect the AP propagation and conduction velocity. Of note, the absolute conduction velocity depends critically on molecular properties such as connexin-encoded gap junction expression; although microgroove-induced directionality may very well affect connexin expression and function, further molecular and cellular investigations will be required. Nonetheless, anisotropy seen in native heart tissue has been clearly reproduced. The difference in AP propagation for the monolayer grown on the control and P5 substrates is more apparent under the isochrone mapping (25 ms intervals). The directed AP propagation and nearly twofold difference between the LCV and TCV suggests the improved functionality of hESC-CMs aligned on the P5 substrate.

The alignment of various cell types including pluripotent hESCs as well as the demonstrated functionality of aligned hESC-CM are some examples of how this substrate can be used to rapidly and easily perform otherwise challenging biological studies. The ability to affect contact guidance of hESCs could elucidate critical molecular pathways and lead to directed differentiation into specific lineages. Our aligned patterned

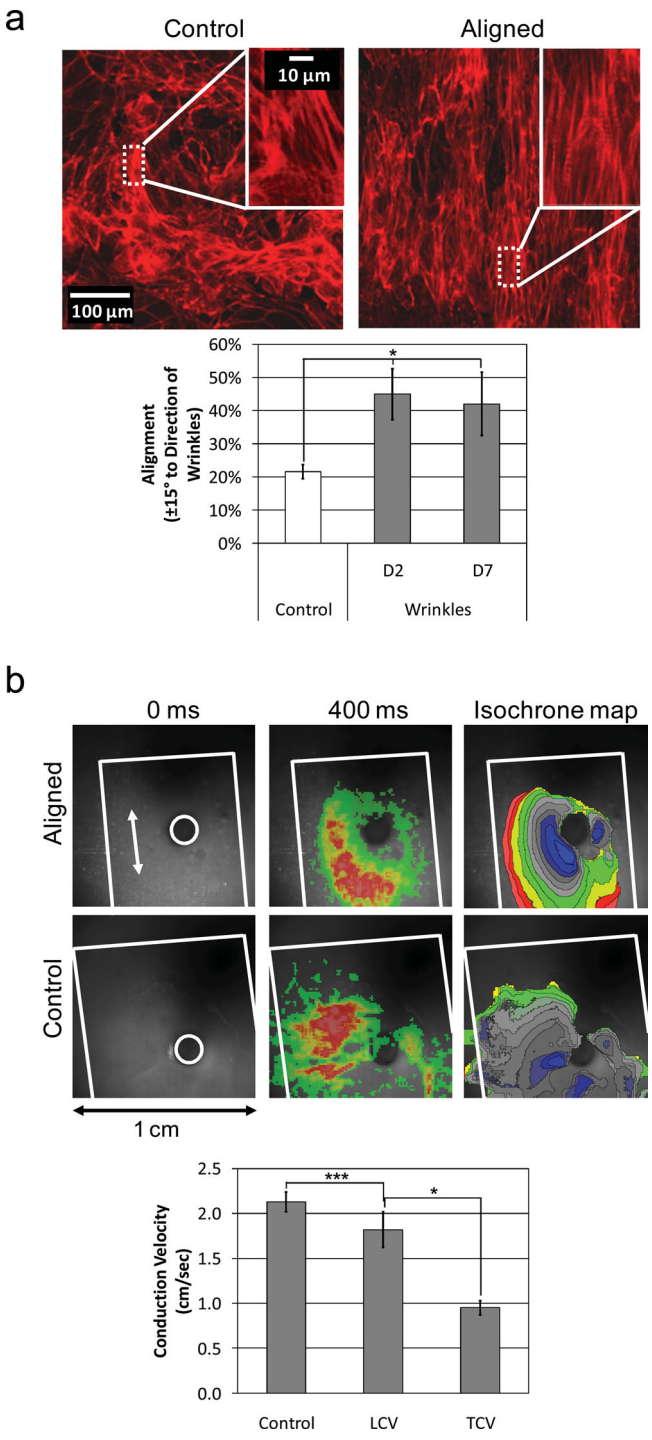

Figure 4. a) Fluorescent microscopy images of hESC-CM cultured on control (P0) and P5 wrinkled substrates for 2 days. Insets represent magnified regions where sarcomeric structures of hESC-CM are compared between conditions. Bar graph (mean ± s.d., $n = 9$ images per time point) represents the percentage of cells aligns to ±15° of the direction of wrinkles. Control is an average of both day 2 and 7 cultures. b) Characterization of electrophysiology of hESC-CM monolayers. Point stimulation (1.5 Hz, 8 V, 20 ms duration), as indicated by the white circle, was applied to the monolayers plated on P0 (control) and P5 (aligned) surfaces. The direction of wrinkles is indicated by the double sided arrows, and the substrate is indicated by the white border. AP propagations at 0 ms and 400 ms are shown, and isochrone maps are spaced at 25 ms intervals. The average conduction velocity for the control is 2.13 ± 0.11 cm s^{-1} ($n = 3$), and the LCV and TCV for the aligned monolayer are 1.82 ± 0.20 cm s^{-1} and 0.95 ± 0.08 cm s^{-1} ($n = 4$), respectively. The ratio of LCV to TCV is about 1.91. $*p < 0.001$ and $***p < 0.05$.

substrates enabled us to reproduce the anisotropy seen in the native heart and are therefore a more accurate in vitro model. Our preliminary data further show that aligned monolayers of hESC-CMs are less susceptible than unaligned controls to sustained reentry arrhythmias (data not shown). Further studies are warranted and may lead to the design of safer grafts with improved efficacy for future clinical applications. Importantly, such a robust, easy to fabricate and configurable platform (compatible with microtiter plates and spatiotemporal imaging/mapping) could enable ubiquitous alignment of any adherent cell type for various tissue engineering and injury repair applications.

Experimental Section

Fabrication of Wrinkled Substrate: Wrinkled substrates were fabricated from PE films (Cryovac D-film, LD935, Sealed Air Corporation). PE film, cut into a 2.5 in. by 5.5 in. strip, was placed lengthwise onto a glass plate. The film was treated with oxygen plasma (Plasma Prep II, SPI Supplies) for 1, 5, or 15 min. After plasma treatment, a PE piece was constrained on opposite sides with binder clips (2 in. binder clips; OfficeMax), and was thermally shrunk at 150 °C for 3 min to generate aligned wrinkles. The PE wrinkled film was trimmed and mounted to a 12 mm glass coverslip (wrinkled substrate) for cellular plating. Wrinkled substrates were sterilized by immersing in 70% ethanol and under UV light for 30 min inside a biosafety cabinet.

Characterization of Wrinkles: To characterize the wrinkles, we performed SEM and AFM. For the SEM, wrinkled substrates were sputter coated (Polaron SC7620) with 3 nm gold/palladium. SEM images were obtained on each wrinkled substrate with 1000, 5000, 10 000, and 20 000 magnifications, 10 kV beam, and 12 mm working distance (Hitachi S-4700-2 FE-SEM Scanning Electron Microscope). Images were analyzed by fast Fourier transform using a MATLAB (MathWorks Inc., Natick, MA, USA) code developed in-house. AFM was conducted on a MFP-3D inverted optical microscope (Asylum Research, Santa Barbara, CA). The topographic of images of the 1, 5, and 15 min plasma treatment substrates were taken in tapping mode. Silicon tips with a resonant frequency of about 75 kHz and force constant of 3 N m^{-1} were used. The software used for data acquisition and analysis was IGOR Pro 6.0 (Wavemetrics, Portland, OR).

Cell Cultures: Details of culturing AoSMC, MEF, and hESC are described in the Supporting Information.

Cell Alignment: In the AoSMC, MEF, and hESC-CM alignment study, cells were loaded onto wrinkled substrates, coated with Matrigel (1:200 dilution) and placed inside a 24-well plate, at a density of 5×10^4 cells per well for both AoSMCs and MEFs, and at a density of 5×10^5 for hESC-CMs. End-point cell staining was performed at 24 h for both AoSMCs and MEFs and at 48 h for hESC-CMs.

The feeder-independent hESC alignment study first required that the wrinkled substrates be coated in Matrigel for a minimum of 24 h. The cell loading density was 5×10^4 cells per well. Daily exchange of hESC conditioned medium was required for culturing the cells. End-point cell staining was performed at nine time points: 0.5, 1, 1.5, 2, 4, 6, 12, 24, and 72 h. Confocal microscopy images (Laser Scanning Microscopy 710, Zeiss) were taken on all samples from each time point for further image analysis.

For the long term culture experiment, feeder-independent hESCs were cultured on both control and wrinkled substrates, coated with

Matrigel and inserted in 6-well culture plates. The cell loading densities were 2.5×10^5 and 1×10^5 cells per well for 3 and 6 day culture, respectively. The medium was exchanged daily but no passaging was performed. Each condition had three replicates, and all replicates were pooled and end-point flow cytometry was performed.

Cardiomyocyte Differentiation: Details are described in the Supporting Information.

Measurement of hESC-CM Electrophysiology: Optical mapping of AP propagation was performed on hESC-CM monolayer by using MiCam Ultima fluorescence imaging system (SciMedia) with a 1 cm^2 field-of-view. The hESC-CMs were cultured on the matrigel-coated P5 substrate for 3 to 4 days to allow establishment of intercellular electrical connections before the imaging measurements. To visualize AP propagation, the hESC-CM monolayer on P5 substrate was first stained with 10 μM voltage-sensitive dye di-4-ANEPPS (Invitrogen) for 5 min at room temperature in Tyrode's solution (140 mM NaCl, 5 mM KCl, 1 mM $MgCl_2$, 1 mM $CaCl_2$, 10 mM glucose, and 10 mM HEPES at pH 7.4). The dye was excited by a halogen light source filtered by a 515 ± 35 nm band-pass filter and emission was filtered by a 590 nm high-pass filter. The cells were stimulated by a coaxial point stimulation electrode at 1.5 Hz, 8 V, and 20 ms pulse duration. Data were collected at room temperature with a sampling rate of 0.2 kHz and analyzed using BV_Ana software (BrainVision, Japan).

Immunostaining, Flow Cytometry, Image Analysis, Statistics: Details are described in the Supporting Information.

Supporting Information

Supporting Information is available from the Wiley Online Library or from the author.

Acknowledgements

M.K. is the scientific founder of Shrink Nanotechnologies, Inc. but receives no compensation nor does she have any financial interest in the company. Terms of this arrangement have been reviewed and approved by UC Irvine in accordance with its conflict of interest policies.

This work was supported in part by The Edwards Lifesciences Center for Advanced Cardiovascular Technology Training Fellowship (A.C.), the California Institute for Regenerative Medicine (Grant#: RN2-00921-1, M.K. and R.A.L.), the NIH Director's New Innovator Award Program (1DP2OD007283, M.K.), Defense Advanced Research Projects Agency (DARPA) N/MEMS S&T Fundamentals Program under grant no. N66001-1-4003 issued by the Space and Naval Warfare Systems Center Pacific (SPAWAR) to the Micro/nano Fluidics Fundamentals Focus (MF3) Center (M.K.), and Shrink Nanotechnologies Inc and the Stanford CIS grant (M.K.). The NIH - R01 HL72857 (R.A.L.), the CC Wong Foundation Stem Cell Fund (R.A.L.) and the Research Grant Council (Project 103544, R.A.L.). Thanks also to Nick Sharac (Regan lab, UCI), Michelle Digman and the Laboratory of Fluorescence Dynamics, and Chuck Hitzman at the Stanford Nanocharacterization Lab.

Received: September 7, 2011
Published online:

[1] C. S. Chen, M. Mrksich, S. Huang, G. M. Whitesides, D. E. Ingber, *Science* **1997**, *276*, 1425.
[2] M. J. Dalby, N. Gadegaard, R. Tare, A. Andar, M. O. Riehle, P. Herzyk, C. D. Wilkinson, R. O. Oreffo, *Nat. Mater.* **2007**, *6*, 997.
[3] D. H. Kim, E. A. Lipke, P. Kim, R. Cheong, S. Thompson, M. Delannoy, K. Y. Suh, L. Tung, A. Levchenko, *Proc. Natl. Acad. Sci. USA* **2010**, *107*, 565.
[4] M. J. Dalby, M. O. Riehle, S. J. Yarwood, C. D. Wilkinson, A. S. Curtis, *Exp. Cell Res.* **2003**, *284*, 274.
[5] A. S. Nathan, B. M. Baker, N. L. Nerurkar, R. L. Mauck, *Acta Biomater.* **2010**, *7*, 57.
[6] F. M. Watt, P. W. Jordan, C. H. O'Neill, *Proc. Natl. Acad. Sci. USA* **1988**, *85*, 5576.
[7] A. J. Engler, S. Sen, H. L. Sweeney, D. E. Discher, *Cell* **2006**, *126*, 677.
[8] B. Murtuza, J. W. Nichol, A. Khademhosseini, *Tissue Eng. Part B Rev.* **2009**, *15*, 443.
[9] S. Pagliari, A. C. Vilela-Silva, G. Forte, F. Pagliari, C. Mandoli, G. Vozzi, S. Pietronave, M. Prat, S. Licoccia, A. Ahluwalia, E. Traversa, M. Minieri, P. Di Nardo, *Adv. Mater.* **2011**, *23*, *514*.
[10] S. Soliman, S. Pagliari, A. Rinaldi, G. Forte, R. Fiaccavento, F. Pagliari, O. Franzese, M. Minieri, P. Di Nardo, S. Licoccia, E. Traversa, *Acta Biomater.* **2010**, *6*, 1227.
[11] E. K. Yim, E. M. Darling, K. Kulangara, F. Guilak, K. W. Leong, *Biomaterials* **2010**, *31*, 1299.
[12] C. J. Bettinger, R. Langer, J. T. Borenstein, *Angew. Chem. Int. Ed.* **2009**, *48*, 5406.
[13] N. Bowden, S. Brittain, A. G. Evans, J. W. Hutchinson, G. M. Whitesides, *Nature* **1998**, *393*, 146.
[14] M. T. Lam, W. C. Clem, S. Takayama, *Biomaterials* **2008**, *29*, 1705.
[15] X. Jiang, S. Takayama, X. Qian, E. Ostuni, H. Wu, N. Bowden, P. LeDuc, D. E. Ingber, G. M. Whitesides, *Langmuir* **2002**, *18*, 3273.
[16] G. D. Pins, D. L. Christiansen, R. Patel, F. H. Silver, *Biophys. J.* **1997**, *73*, 2164.
[17] G. C. Engelmayr, Jr., M. Cheng, C. J. Bettinger, J. T. Borenstein, R. Langer, L. E. Freed, *Nat. Mater.* **2008**, *7*, 1003.
[18] C. C. Fu, A. Grimes, M. Long, C. G. L. Ferri, B. D. Rich, S. Ghosh, S. Ghosh, L.P. Lee, A. Gopinathan, M. Khine, *Adv. Mater.* **2009**, *21*, 4472.
[19] J. I. Luna, J. Ciriza, M. E. Garcia-Ojeda, M. Kong, A. Herren, D. Lieu, R. A. Li, C. C. Fowlkes, M. Khine, K. E. McCloskey, *Tissue Eng. C* **2011**, *17*, 579.
[20] K. Efimenko, J. Finlay, M. E. Callow, J. A. Callow, J. Genzer, *ACS Appl. Mater. Interfaces* **2009**, *1*, 1031.
[21] S. Gerecht, C. J. Bettinger, Z. Zhang, J. T. Borenstein, G. Vunjak-Novakovic, R. Langer, *Biomaterials* **2007**, *28*, 4068.
[22] M. A. Laflamme, K. Y. Chen, A. V. Naumova, V. Muskheli, J. A. Fugate, S. K. Dupras, H. Reinecke, C. Xu, M. Hassanipour, S. Police, C. O'Sullivan, L. Collins, Y. Chen, E. Minami, E. A. Gill, S. Ueno, C. Yuan, J. Gold, C. E. Murry, *Nat. Biotechnol.* **2007**, *25*, 1015.
[23] K. R. Stevens, K. L. Kreutziger, S. K. Dupras, F. S. Korte, M. Regnier, V. Muskheli, M. B. Nourse, K. Bendixen, H. Reinecke, C. E. Murry, *Proc. Natl. Acad. Sci. USA* **2009**, *106*, 16568.
[24] C. Xu, M. S. Inokuma, J. Denham, K. Golds, P. Kundu, J. D. Gold, M. K. Carpenter, *Nat. Biotechnol.* **2001**, *19*, 971.
[25] A. D. van der Meer, A. A. Poot, J. Feijen, I. Vermes, *Biomicrofluidics* **2010**, *4*, 11103.
[26] M. J. Dalby, N. Gadegaard, P. Herzyk, D. Sutherland, H. Agheli, C. D. Wilkinson, A. S. Curtis, *J. Cell Biochem.* **2007**, *102*, 1234.
[27] J. D. Pajerowski, K. N. Dahl, F. L. Zhong, P. J. Sammak, D. E. Discher, *Proc. Natl. Acad. Sci. USA* **2007**, *104*, 15619.
[28] L. E. McNamara, R. J. McMurray, M. J. P. Biggs, F. Kantawong, R. O. C. Oreffo, M. J. Dalby, *J. Tissue Eng.* **2010**, *2010*, 1.
[29] H. T. Au, I. Cheng, M. F. Chowdhury, M. Radisic, *Biomaterials* **2007**, *28*, 4277.
[30] H. T. Heidi Au, B. Cui, Z. E. Chu, T. Veres, M. Radisic, *Lab Chip* **2009**, *9*, 564.
[31] T. Xue, H. C. Cho, F. G. Akar, S. Y. Tsang, S. P. Jones, E. Marban, G. F. Tomaselli, R. A. Li, *Circulation* **2005**, *111*, 11.
[32] L. Yang, M. H. Soonpaa, E. D. Adler, T. K. Roepke, S. J. Kattman, M. Kennedy, E. Henckaerts, K. Bonham, G. W. Abbott, R. M. Linden, L. J. Field, G. M. Keller, *Nature* **2008**, *453*, 524.